Journal of Materials Processing Tech. 339 (2025) 118823

Contents lists available at ScienceDirect

Journal of Materials Processing Tech.

journal homepage: www.elsevier.com/locate/jmatprotec

Research Article

Effect of shot peening temperature on the microstructure induced by surface severe plastic deformation on an austenitic stainless steel

Yann Austernaud [a,b,c,*], Marc Novelli [a,b,*], Philippe Bocher [c], Thierry Grosdidier [a,b]

[a] Laboratoire d'Etude des Microstructures et de Mécanique des Matériaux (LEM3), UMR CNRS 7239, 7 rue Félix Savart, BP 15082, Metz F-57073, France
[b] LABoratoire d'Excellence Design des Alliages Métalliques pour Allègement des Structures (DAMAS), Université de Lorraine, Metz F-57045, France
[c] Laboratoire d'Optimisation des Procédés de Fabrication Avancés (LOPFA), Ecole de technologie supérieure, 1100 rue Notre Dame Ouest, Montréal H3C 1K3, Canada

ARTICLE INFO

Keywords:
Surface mechanical attrition treatment (SMAT)
Austenitic stainless steel
Warm deformation
Gradient microstructure

ABSTRACT

The mechanisms of microstructure modifications were investigated for a 316 L austenitic stainless steel subjected to Surface Mechanical Attrition Treatment (SMAT) across a wide temperature range (143 K to 773 K) and their effects on hardness and residual stresses evolutions determined. The research highlights how temperature modulates deformation mechanisms, transitioning from Transformation-Induced Plasticity (TRIP) and Twinning-Induced Plasticity (TWIP) at low temperatures to dislocation glide and dynamic recrystallization at elevated temperatures. These transitions lead to a distinct trade-off: while cryogenic SMAT enhances surface hardness and compressive residual stresses, warm SMAT, particularly at 773 K, facilitates the formation of a thick refined surface layer due to thermal softening effect and increases the deformation and residual stress gradient depth. This study provides new insights into tailoring surface properties through controlled temperature during SMAT, offering pathways to enhance mechanical performance for advanced applications.

1. Introduction

Industry requires high-strength materials to fit with complex specifications. A way to improve material mechanical properties is the reduction of grain size through grain refinement, which can be achieved by Severe Plastic Deformation (SPD). Applied to bulk parts, SPD processes such as Equal Chanel Angular pressing (ECAP) or High Pressure Torsion (HPT) for example, allow to refine significantly the overall microstructure of a material but can hardly be scaled up to industrial applications due to the high load required and the geometry of material parts [1]. Comparatively, as surface state plays a key role in controlling the failure process of a mechanical part, surface optimisation by SPD is often sufficient to improve the overall behaviour and durability of an engineering component via the formation of a gradient microstructure [2].

Different Surface Severe Plastic Deformation (SSPD) processes have been developed to modify the surface of a material. They generate compressive residual stresses and microstructure gradients consisting of surface ultrafine grains and subsurface fine grains [3]. The plastic deformation can be imparted to the surface by energetic beams such as laser beams [4] or pulsed electron beams [5], or by mechanical impacts [6]. Among the mechanical impact SSPD technics, Surface Mechanical Attrition Treatment (SMAT) - sometimes referred as to Ultrasonic Shot Peening (USP) - uses shots set in motion in a confined chamber impacting the sample surface with a wide variety of incidence angles. This enables to refine more efficiently the microstructure than other mechanical processes derived directly from shot peening in which single-incidence impact angles are involved [7,8]. SMAT induces high strain and strain rates at the sample surface, which then decrease with distance from the surface. The high strain and the strain rate reached at

---

Abbreviations: CDRX, continuous Dynamic Recrystallization; CSL, Coincidence Site Lattice; CT, Cryogenic Temperature; DDRX, discontinuous Dynamic Recrystallization; DRX, Dynamic Recrystallisation; EBSD, Electron BackScatter Diffraction; ECAP, Equal Chanel Angular pressing; FWHM, Full Width at Half Maximum; GND, Geometrically Necessary Dislocation; HPT, High Pressure Torsion; IPF, Inverse Pole Figure; OR, Orientation Relationship; PDL, Plastically Deformed Layer; RT, Room Temperature; SAM, Stress Assisted Martensite; SEM, Scanning Electron Microscopy; SFE, Stacking Fault Energy; SIM, Strain Induced Martensite; SMAT, Surface Mechanical Attrition Treatment; SPD, Severe Plastic Deformation; SSPD, Surface Severe Plastic Deformation; TKD, Transmission Kikuchi Diffraction; TL, Transition Layer; TRIP, Transformation Induced Plasticity; TWIP, Twinning Induced Plasticity; UFG, Ultra Fine Grains; USP, Ultrasonic Shot Peening.

* Corresponding authors at: Laboratoire d'Etude des Microstructures et de Mécanique des Matériaux (LEM3), UMR CNRS 7239, 7 rue Félix Savart, BP 15082, Metz F-57073, France.

E-mail addresses: yann.austernaud@univ-lorraine.fr (Y. Austernaud), marc.novelli@univ-lorraine.fr (M. Novelli).

https://doi.org/10.1016/j.jmatprotec.2025.118823
Received 12 November 2024; Received in revised form 20 March 2025; Accepted 20 March 2025

the surface can potentially lead to the formation of a nanostructured layer [8,9]. The efficiency of these peening treatments depends directly on the processing parameters controlling the mechanical energy transferred to the material via the impacts of the shots. An additional parameter is the temperature at which the peening is done as the temperature influences the response of the material by modifying its strength and, possibly, the types of deformation mechanisms being active [10]. As the strength of industrial materials is usually quite high for design purposes, it becomes more difficult to use the impact energy from shots to deform these already hard materials, as a significant part of the deformation generated during the impact is imparted to the shots. In some materials, such as superalloys or martensitic steels, the highly deformed layer formed at the upper surface by SSPD can inhibit the sub-surface deformation and thus limit the depth to which the process can affect the material [10]. Increasing impact energy (i.e. shot velocity or shot size) to better deform hard materials can introduce cracks at the surface that will affect the surface integrity of the material [11,12]. A way to deal with these limits is to increase the processing temperature [10,13]. Heating the part decreases the flow stress of the material and then allows the transfer of more mechanical energy to the material.

Warm shot peening was introduced by Tange *et al.* to refine the microstructure of a spring steel (SUP7) and to improve coils properties for automotive applications [14]. Warm peening has been applied mainly on hard cast steels [15,16], hard martensitic stainless steels [17] or titanium alloys [18,19] to improve energy transfer and efficiently deform the microstructure below the surface. Different ways can be used to change the temperature of SSPD processes. Peening can be done directly in a furnace [14,20], by heating samples via a hot plate [21,22], via joule effect [23], or by radiation [24,25]. New microstructures can be created as a result of the recovery process during warm peening processes. For example, Tange *et al.*, explained the hardness increase of a warm peened SUP7 Steel through dynamic strain aging and Cottrell effect [14] while Ye *et al.* have documented dynamic precipitation under warm SSPD in aluminium alloys [26]. Dynamic recrystallisation can also take place under warm severe plastic deformation in titanium and Fe-Cr alloys [27,28]. These various mechanisms have to be well documented, and their interaction taken into consideration in order to optimise the process of severe plastic deformation.

The accommodation of deformation, dislocation evolution and related microstructures of austenitic stainless steels depend critically on Stacking Fault Energy (SFE) which reflects the ease of a dislocation to dissociate in Shockley partial dislocations. At high SFE, typically $> 50\,\mathrm{mJ.m^{-2}}$ in a 316 L, the dissociation of a perfect dislocation in highly unlikely and the material relies only on dislocation glide to accommodate plastic deformation. If the SFE decreases in a certain range, $15 \sim 50\,\mathrm{mJ.m^{-2}}$, dislocation dissociation will be promoted leading to the nucleation and growth of mechanical twins by the insertion of partial dislocations on every dense plane of the twinned volume. However, when the SFE is lower than a critical value, $< 15\,\mathrm{mJ.m^{-2}}$, the probability of missing the emission of one of the partial dislocations on a plane in the twinned volume increases leading to the formation of the ε-martensite by the insertion of partial dislocation every two dense planes [29]. Austenitic stainless steels have a wide range of SFE value depending on their composition and the temperature [30,31]. Thus, the temperature at which the deformation is applied is of great importance as it will drive the deformation accommodation mechanisms and the related mechanical properties.

SMAT at Room Temperature (RT) [32,33] has improved the fatigue life of various stainless steel [34,35]. The effect of the cryogenic peening temperature was limited in a stable stainless steel such as the 310 L (high SFE). Comparatively, for the metastable 304 L (low SFE), cryogenic temperature promotes the formation of martensite. The formation of Strain Induced Martensite (SIM) at the surface and Stress Assisted Martensite (SAM) in the subsurface region resulted in an efficient in-depth hardening compared to smaller amount of SIM martensite formed at RT [36]. An intermediate SFE alloy, such as the 316 L, can cover a wide range of deformation mechanisms by changing the process temperature and was selected for the present study in order to investigate the possibility to generate different types of microstructure gradients under SSPD.

Despite significant advancements in modelling of SMAT process [37], or in the use of peening process to optimize microstructure obtained from additive manufacturing [38], the role of the peening temperature in governing deformation mechanisms and microstructural gradients during SSPD in metastable austenitic stainless steels remains poorly understood. Existing studies primarily focus on room or cryogenic temperatures, with limited exploration of elevated-temperature regimes. The present study addresses these gaps by systematically investigating the effect of SMAT temperature, ranging from cryogenic conditions to 773 K. The different mechanisms accommodating the deformation at different SMAT temperatures are documented using electronic imaging and diffraction along the affected gradient and then used to explained the related gradient properties in terms of hardness and residual stresses.

2. Material and methods

2.1. Material and surface treatment parameters

A 316 L austenitic stainless steel with the chemical composition given in Table 1 was used in this study. The Martensite Start temperature (M_s) and M_{d30} temperature (the temperature for which 50 % of martensite has formed for a 30% applied strain) of the studied 316 L are estimated to be 88 K and 278 K, respectively, as calculated using the formulations (1) and (2) from the work of Pickering [39] and Angel [40] (element amount in wt%), respectively.

$$Ms(K) = 778 - 810\%C - 1230\%N - 13\%Mn - 30\%Ni - 12\%Cr - 54\%Cu - 46\%Mo\# \tag{1}$$

$$Md_{30}(K) = 686 - 462(\%C + \%N) - 9.2\%Si - 8.1\%Mn - 13.7\%Cr - 9.5\%Ni - 18.5\%Mo\# \tag{2}$$

Cylindrical specimens having a 6 mm gauge diameter were subjected to SMAT using a Sonats Stressonic© apparatus [41] to which was attached to an in-house developed devices allowing to heat up or cool down the samples. Fig. 1a represents the thermomechanical cycles used during SMAT and Fig. 1b,c are schematic representations of the cryogenic and warm setups, respectively. In order to cooldown the specimen

Table 1

chemical composition [wt%] of the 316 L austenitic stainless steel studied.

Element	C	Cr	Ni	Mo	Mn	Si	N	P	Fe
Composition [wt%]	0.02	16.6	10.0	2.1	1.3	0.4	0.05	0.03	bal.

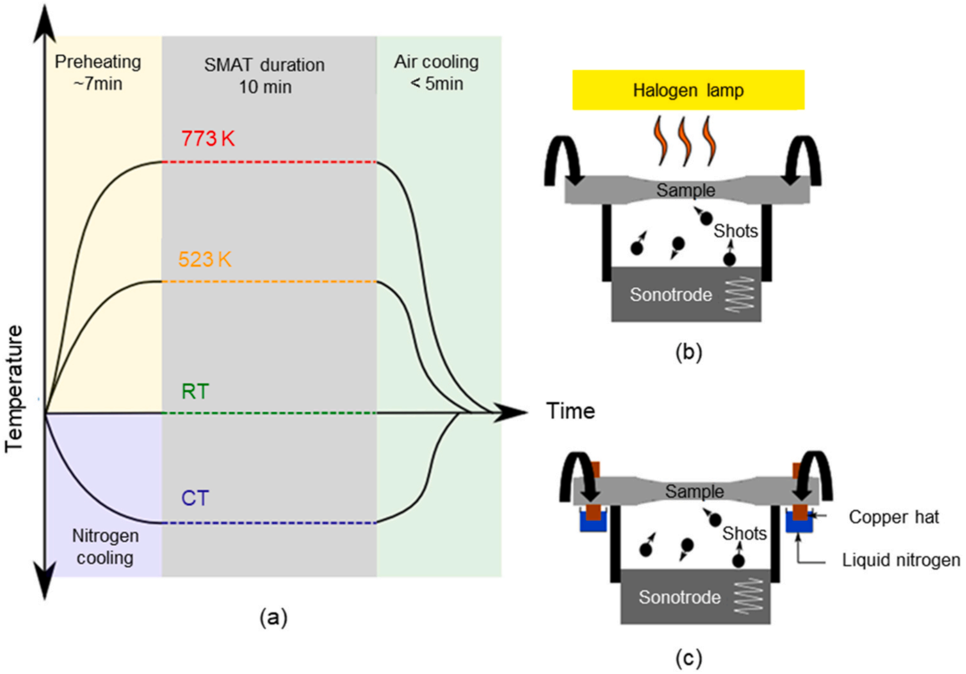

Fig. 1. (a) Thermomechanical cycles used during SMAT in temperature and schematic representations of the (b) warm and (c) cryogenic setups.

to cryogenic temperature (Fig. 1c), copper hats were attached to the specimen heads and partially immersed in liquid nitrogen. The heating device (Fig. 1b) consisted of an elliptical furnace focusing a halogen lamp radiation to the specimen surface. The specimens were pre-heated/-cooled at the desired temperatures and kept in temperature for 7 min before starting SMAT for 10 min. Finally, the power was turned off or the liquid nitrogen evacuated to let the sample reach room temperature within less than 5 min. The SMAT was carried out using a sonotrode vibrating with a frequency of 20 kHz and an amplitude of 60 µm. A mass of 4.2 g (~130 shots) of 100C6 shots having a diameter of 2 mm was inserted in the chamber and the specimen set in rotation at 10 rpm before starting the surface treatment.

Only the temperature was used as a treatment variable. The specimens were SMATed under four temperature conditions: cryogenic temperature (~ 143 K, CT), RT (293 K), 523 K, and 773 K. At these temperatures, the SFEs are estimated to be 6, 23, 44, and 69 $mJ.m^{-2}$, respectively; according to the formulation proposed by Bellefon and van Duysen (Eq. 3) [42] for the RT value and the linear dependency with temperature of 0.1 $mJ.m^{-2}.K^{-1}$ estimated by Rémy et al. [43].

$$\mathrm{SFE}\left(\mathrm{mJ.m}^{-2}\right) = 2.2 + 1.9\%Ni - 2.9\%Si + 0.77\%Mo + 0.5\%Mn + 40\%C - 0.016\%Cr - 3.6 \tag{3}$$

2.2. *Surface and sub-surface analyses*

Roughness was measured using Mitutoyo SJ-400 profilometer with a cut off λ_c of 2.5 mm and an evaluation length set at 12.5 mm, following ISO4287. Values and related errors are the mean values and the standard deviations calculated on 10 measurements.

For cross-section microstructural observations, samples were nickel-plated in a Watts bath to prevent edge effect during polishing. Samples were then mirror-polished from 320 SiC paper down to OPS before electronic imaging. The microstructures were investigated by Scanning Electron Microscopy (SEM) imaging as well as Electron BackScatter Diffraction (EBSD) and Transmission Kikuchi Diffraction (TKD) using a Zeiss SUPRA 40 and Jeol F100 SEM, respectively. EBSD maps were acquired at different depths with an acceleration tension of 15 kV and a step size of 50 nm. TKD was also conducted to get further details on the first microns under the deformed surface. Thin blades were extracted by focused ion-beam in cross-section and then subjected to TKD with an acceleration tension of 30 kV and a step size of 10 nm. EBSD and TKD acquisitions were then post-treated with the ATEX software [44]. To document the heterogeneity of deformation in the microstructure, additional maps showing the Geometrically Necessary Dislocation (GND) density were generated. The lattice curvature was calculated from pixel to pixel to deduce the Nye's dislocation density tensor. The entrywise norm of Nye's dislocation density tensor divided by the length of the Burgers vector is then used as an estimation of the GND density [45].

The Vickers hardness gradients were measured on cross section using a CLEMEX Microhardness tester with a step size of 50 µm, a load of 50 gf and a holding time of 10 s. Surface hardness were obtained with the same hardness test parameters (50 gf) directly on the treated surfaces. A brief electropolishing was made to remove the oxide layer formed after the two warm treatments. According to ISO6507–1, it must be considered that hardness indentation on non-planar surfaces may bring measurement errors. Taking the indent diagonal d equal to 16 µm, two cases can be considered here: i) the gauge section having a convex cylindrical surface with a curvature radius D of 3 mm leading to a hardness error lower than 1 % or 5 HV ($d/D = 0.005$) and ii) a shot indent having a concave spherical surface with a curvature radius of 1 mm leading to a hardness error of −2 % or −10 HV ($d/D = 0.016$). Values and related error bars are the mean values and the standard deviations calculated on 10 measurements.

Residual stress gradients were measured using the cos(α) method on a Pulstec µ360 X-ray diffraction instrument with a chromium source, a voltage of 30 kV, a current of 1.5 mA and a collimator diameter of 1 mm. The calculations were made on the $\{311\}\gamma$ austenite (Cr-$K_\beta = 2.085$ Å) and the $\{211\}_{\alpha'}$ martensite (Cr-$K_\alpha = 2.291$ Å) peaks. Only the sample SMATed under cryogenic condition allowed measurements both in the austenite ($2\theta = 152^\circ$) and the martensite ($2\theta = 156\ ^\circ$) when two diffraction peaks were well-defined and their peak fitting was possible. The calculations were performed using the Pulstec software by excluding the martensite peak for austenite and vice versa.

The gradients were acquired by successive electropolishing matter removal using an A3 (5 % perchloric acid, 60 % methanol and 35 % butoxyethanol) solution, then the removed depth was measured using a contact profilometer. A value correction was used to account for the stress relaxation induced by matter removals using the method proposed by Moore and Evans [46] for cylindrical bars. For each XRD profiles measured, the Full Width at Half Maximum (FWHM) was also extracted as it is a representation of the variations of dislocation densities and coherently diffracting domain sizes. Values and related error bars given in the article are the mean values and the standard deviations calculated on 5 measurements made at different points on the specimen circumference.

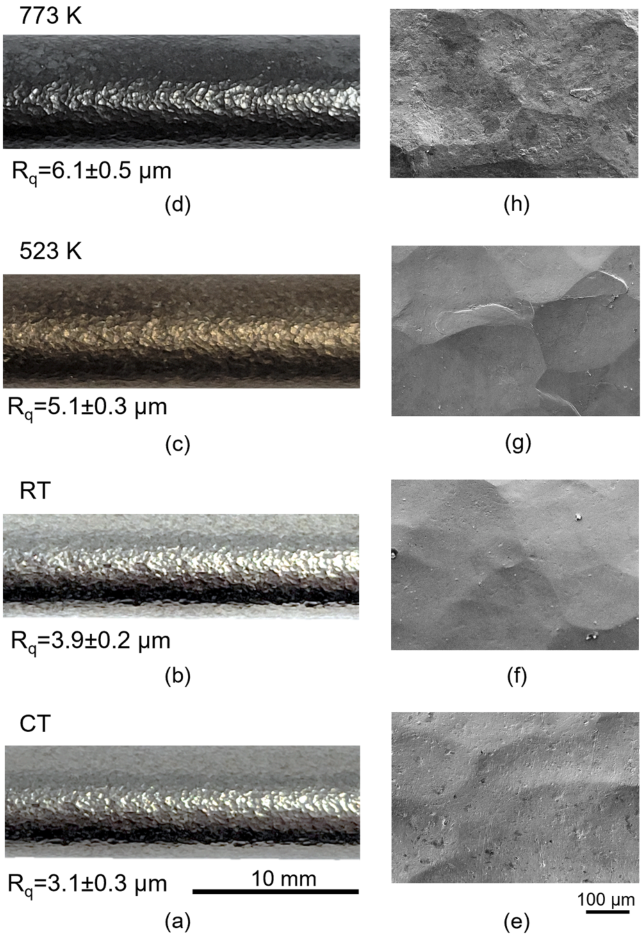

Fig. 2. (a-d) Optical observations of the sample surfaces after SMAT at (a) CT, (b) RT, (c) 523 K, and (d) 773 K. (e-h) SEM surface close views of the sample surfaces after SMAT at (e) CT, (f) RT, (g) 523 K, and (h) 773 K. The corresponding R_q roughness criteria is given for each condition. Error represent ± 1 standard deviation from the mean value (n = 10). (a-d) share the same scale as (a) and (e-h) the one in (e).

3. Results

3.1. Surface observations

The samples subjected to SMAT exhibited a characteristic surface aspect made of impacts resulting from peening. Under both CT and RT conditions, the surfaces display a shiny appearance (Fig. 2a,b). In contrast, at 523 K and 773 K, the samples show brown and bluish colours (Fig. 2c,d), which are attributed to the oxidation occurring during the thermomechanical processing done in temperature under air. Beyond the change in surface appearance, increasing the treatment temperature resulted in deeper craters formed by shot impacts (Fig. e-h), leading to a rise in surface roughness from 3.1 µm at CT to 6.1 µm at 773 K.

3.2. Microstructure observations

The microstructures formed by SMAT are usually described as a succession of three different layers. An Ultra Fine Grains (UFG) layer, close to the surface, having sub-micrometric size grains. Deeper in the gradient, the Transition Layer (TL) containing grains that were undergoing the refinement process. Finally, the Plastically Deformed Layer (PDL) where the grains are comparable in size as in the undeformed core and the occurrence of plastic deformation is witnessed by the presence of intragranular misorientation or twins.

The low magnification images of the SMATed samples cross-sections for the different treatment temperatures reveal such an evolution of microstructure as depicted in Fig. 3. The initial large, undeformed grains in the core of the samples become more subdivided and fragmented when approaching the treated surface. The low magnification in Fig. 3 is not sufficient to depict the UFG zone, but the dimension of the UFG+TL can be roughly estimated (dashed black arrows in Fig. 3) to be 180, 200, 220, and 250 µm after SMAT at CT, RT, 523 K, and 773 K, respectively. Below this depth, the initial recrystallised grains (having grain size in the range 20–60 µm) exhibit contrast variations witnessing intergranular misorientations. Based on the presence of intragranular misorientations, the thicknesses of the PDL were estimated (black arrows) to be 210, 290, 380, and 450 µm after SMAT at CT, RT, 523 K, and 773 K, respectively. Thus, increase the SSPD treatment temperature leads to an increase of the overall affected depth by increasing both the UFG+TL and PDL thicknesses.

Fig. 4 presents high magnification observations of the microstructure at different depths for the CT and 773 K samples. Both samples show extremely refined microstructures at the extreme surface (Fig. 4a,b) and at a depth of 50 µm (Fig. 4c,d). Even though the microstructures generated at 773 K remain very small, they are still coarser than the CT SMAT ones. At a depth of 200 µm (Fig. 4e,f), planar defects subdivide the initial coarse grains of the CT SMATed sample whereas strong intragranular disorientation contrasts can be seen in the microstructure of the sample SMATed at 773 K. The maximum affected depth seems to be reached at 400 µm under CT SMAT as no more deformation accommodation defects can be seen (Fig. 4g). Comparatively, the warm deformed sample still shows significant intragranular disorientation at the same depth (Fig. 4h).

Cross-sectional EBSD maps of the first 50 µm under the SMATed

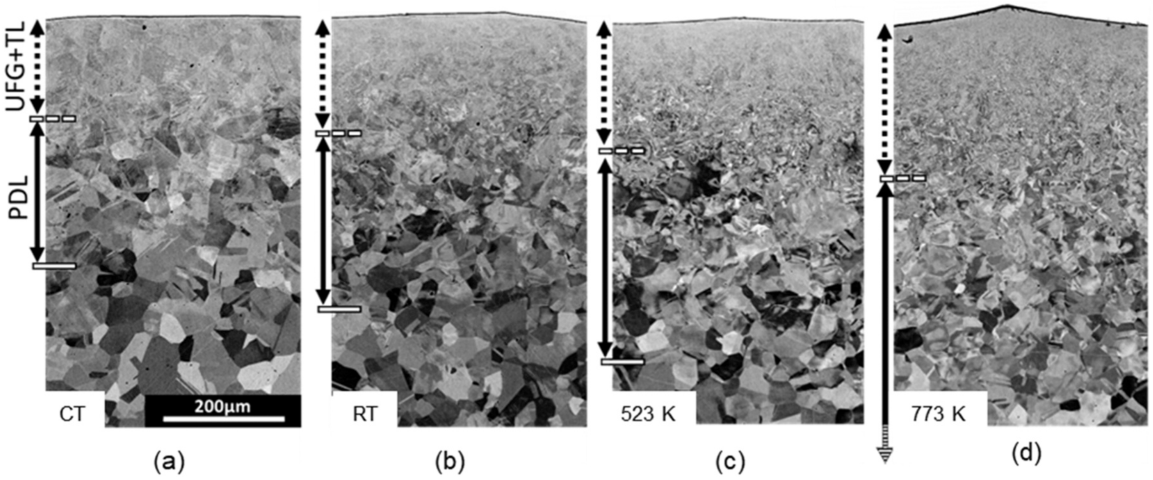

Fig. 3. SEM images of the sample cross-sections after SMAT at (a) CT, (b) RT, (c) 523 K, and (d) 773 K with the treated surface at the top. The vertical black dashed lines roughly estimate UFG + TL thicknesses. The vertical black arrows indicate the estimated thicknesses of the PDL layers. All the images share the same scale given in Fig. 3a.

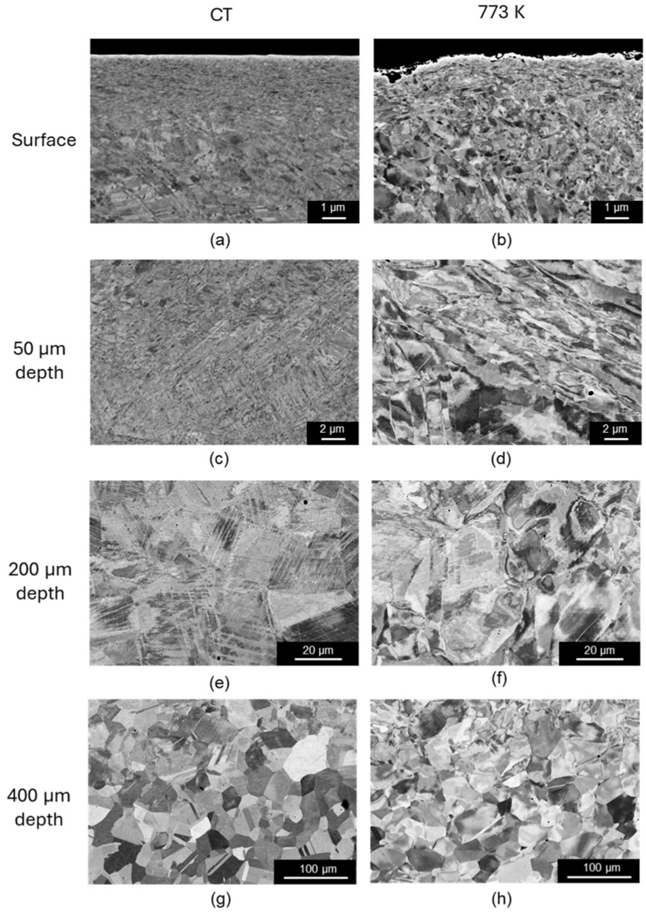

Fig. 4. Higher magnification SEM images of the sample cross-sections after SMAT at (a, b) the surface, (c, d) 50 µm, (e, f) 200 µm, and (g, h) 400 µm under the treated surface for the sample SMATed at (a, c, e, g) CT and (b, d, f, h) 773 K.

surface are displayed in Fig. 5 for the different temperatures. Fig. 5a,c,e, and g are Inverse Pole Figure (IPF) projected on the Z-axis normal to the surface. Fig. 5b,d,f, and h are the corresponding phase maps with the austenite represented in band contrast, the α'-martensite in blue, and the 60° {111} twin boundary in red.

Only the cryogenic SMATed sample (Fig. 5a,b) displays a 18 % amount of α'-martensite (for an overall indexation rate of 90 %) whereas the others either show only a very small amount or no martensite at all. After a cryogenic SMAT, the α'-martensite is located in straight bands within the grains, indicating a deformation induced transformation. A fairly small amount of boundary lengths was indexed as twin boundaries (9.8 % length fraction of the total >5° detected boundaries). When the treatment is carried out at RT (Fig. 5c,d), only 1 % of α'-martensite is detected and a notably higher fraction of twin boundaries was indexed (59 % of length fraction). Additionally, colouration gradients can be seen within the grains (Fig. 5c) reflecting the activity of dislocations leading to intragranular misorientations. Increasing the treatment temperature to 523 K (Fig. 5e,f) completely inhibits the martensitic transformation and leads to a lower fraction of twin boundaries (34 %) (Fig. 5f). The high amount of intragranular misorientation (Fig. 5e) is similar to the RT SMATed sample, with a thicker grain refinement produced at the surface. Finally, when the temperature is further increased to 773 K (Fig. 5g,h), the microstructure differs significantly from the other samples: most of the observed sub-surface consists of ultra-fine grains with a mean size of 0.83 µm over the first 35 µm and only 6.6 % of twin boundary length was indexed on the map. Based on the criteria proposed by Samih *et al.* [47], grain sizes lower than 0.2 µm and 1 µm were used to determine the thicknesses of the nanostructured and UFG layers thicknesses, respectively, from the EBSD data. The nanostructured layer thicknesses are estimated to be 2.8, 1.4, 4.6, and 8.3 µm and the UFG layer thicknesses 4.7, 1.4, 8.3, and 35.3 µm for the CT, RT, 523 K, and 773 K treatment temperatures respectively.

TKD observations had to be used to depict the microstructure over the first microns, as the EBSD pattern indexation is affected by the severe plastic deformation (blurry diffraction patterns) and the potential presence of several phases (diffraction patter superpositions). Fig. 6a,c are IPF projected on the Z-axis of the sample SMATed at CT and 773 K, respectively, and Fig. 6b,d are the corresponding phase maps where the austenite is plotted in band contrast and the α'-martensite in blue. No ε-martensite was indexed in both conditions. The two extreme surface microstructures show equiaxed nanograins, whether the peening was done at CT or under the warm condition of 773 K. The grain size remains comparable between the samples, varying from 55 nm to 67 nm under CT and 773 K, respectively. Only the sample treated at CT shows the presence of α'-martensite (2.5 %), the size of the α'-martensite being comparable to the size of the austenite nanograin and about 60 nm. Twin boundaries relationships were detected under the warm condition at 773 K. They are displayed in Fig. 6d with a tolerance angle of 5° in red

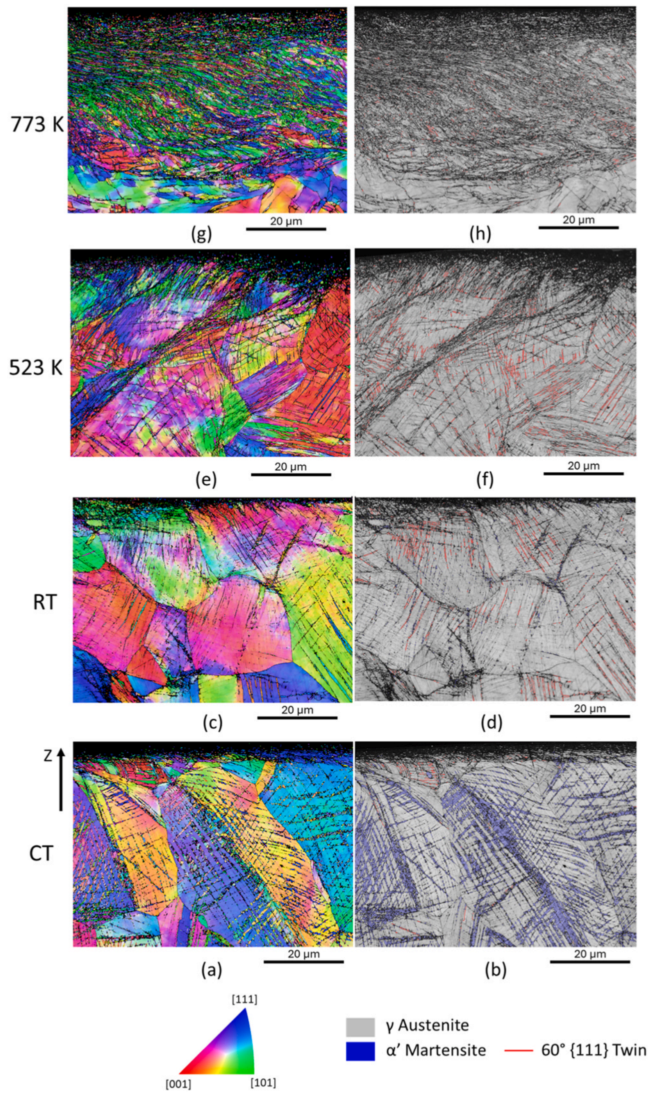

Fig. 5. EBSD maps of the first 50 μm after SMAT at (a, b) CT, (c, d) RT, (e, f) 523 K, and (g, h) 773 K. (a), (c), (e) and (g) are IPF representations along the Z-axis (normal to the observation plane); (b), (d), (f), and (h) are phase maps with the γ austenite in band contrast, the α'-martensite in blue and the 60° {111} twin boundary in red.

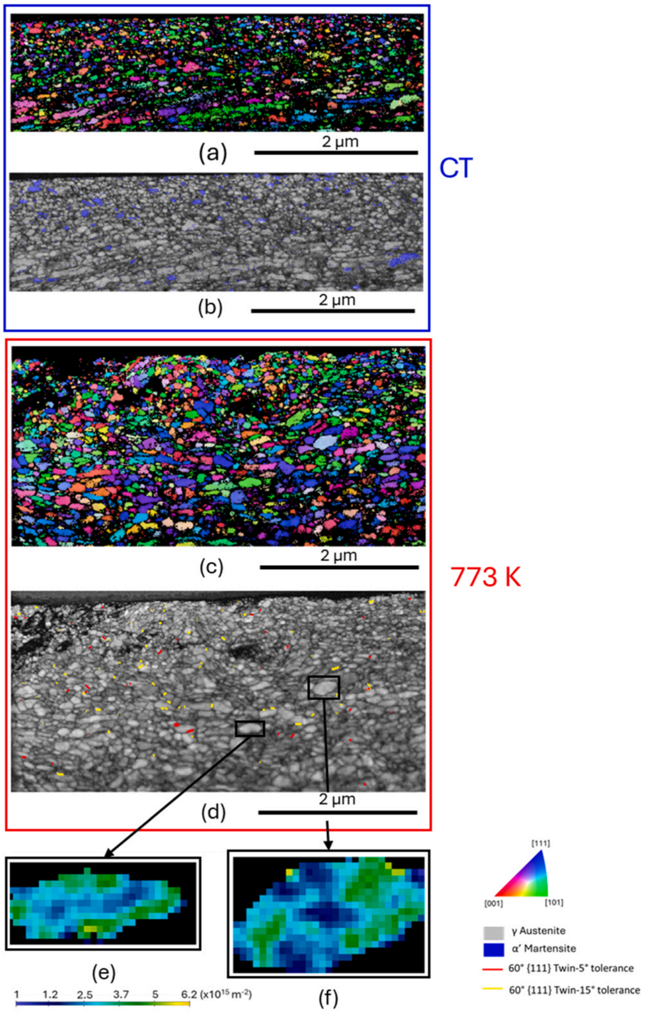

Fig. 6. TKD acquisitions of the UFG region at the extreme surfaces after SMAT at (a, b) CT and (c, d) 773 K: (a), (c) are IPF representations along the Z-axis (normal to the observation plane); (b), (d) are phase maps with the γ austenite in band contrast and the α'-martensite in blue. Grain boundaries with a twin orientation were identified in d with the red and yellow colours based on their tolerance angles. (e); (f) corresponds to close views (black rectangles in Fig. 6d) plotted in GNDs density to show dislocation substructures present inside nanograins.

and 15° in yellow. Note that twin boundaries could not be revealed properly at CT (Fig. 6b) due to the lower indexation rate. The presence of twin boundaries having a good match with some being parallel to each other and numerous others moderately misoriented from the Coincidence Site Lattice (CSL) condition (5–15° from the 60°{111}) suggests the formation and deformation of growth twins during the SMAT process. The growth twins would nucleate from highly misoriented mobile substructures generated during the deformation and restoration processes, but these grains will progressively rotate and lose the CSL relation as they undergo further deformation due to the ongoing SMAT process. Fig. 6e,f are close views of two selected grains (black rectangles in Fig. 6d) plotted with GNDs density contrasts. The GND density plot reveals the formation of dislocation substructures inside the nanograins containing high GND density, while other regions display much lower dislocation density.

In order to document the deformation mechanisms at a depth below 100 μm from the SMATed surface, additional EBSD maps were produced for the CT, RT, and 773 K conditions. For the CT sample, the α'-martensite (in blue) and the ε-martensite (in green) are identified in Fig. 7a. The α'-martensite bands (40 % with overall indexation rate of 90 %) are mostly aligned in specific directions with some intersecting each other whereas the ε-martensite (5.7 %) is located within the α'-martensite bands. The pole figures related to these phases are given in Fig. 7b,c with the γ-austenite plotted in grey, the α'-martensite in blue and the ε-martensite in green. Fig. 7b shows the superposition of the $\{111\}_\gamma$ (grey) and $\{0002\}_\varepsilon$ (green) pole figures. The austenite phase can be interpreted as the parent grain (square markers) containing mechanical twins (star markers). The two dashed lines in Fig. 7b are the two $\{111\}_\gamma$ plane traces having the highest Schmid's factor in the austenite phase assuming compression loading. They correspond to the morphology of the two-plane traces found on the microstructure map, showing that two most activated slip systems correspond to the direction along which the α'-martensite bands preferentially form (Fig. 7a). The superposition of the $(\bar{1}11)_\gamma$ pole with the $(0002)_\varepsilon$ pole in Fig. 7b supports the $(\gamma/\varepsilon)\{111\}_\gamma//\{0002\}_\varepsilon$ $<1\bar{1}0>_\gamma//<11\bar{2}0>_\varepsilon$ Nishiyama Orientation Relationship (OR). Fig. 7c shows also the superposition of one $\{111\}_\gamma$ (grey) and one $\{110\}_{\alpha'}$ (blue) poles. The small circle markers refer to the $\{110\}_{\alpha'}$ poles coming from the 24 variants respecting the possible (γ/α') $\{111\}_\gamma//\{110\}_{\alpha'}$ $<1\bar{1}0>_\gamma//<1\bar{1}1>_{\alpha'}$ Kurdjomov-Sachs OR. Additionally, the $(0002)_\varepsilon$ and $(110)_{\alpha'}$ poles are at the same location (Fig. 7b,c)

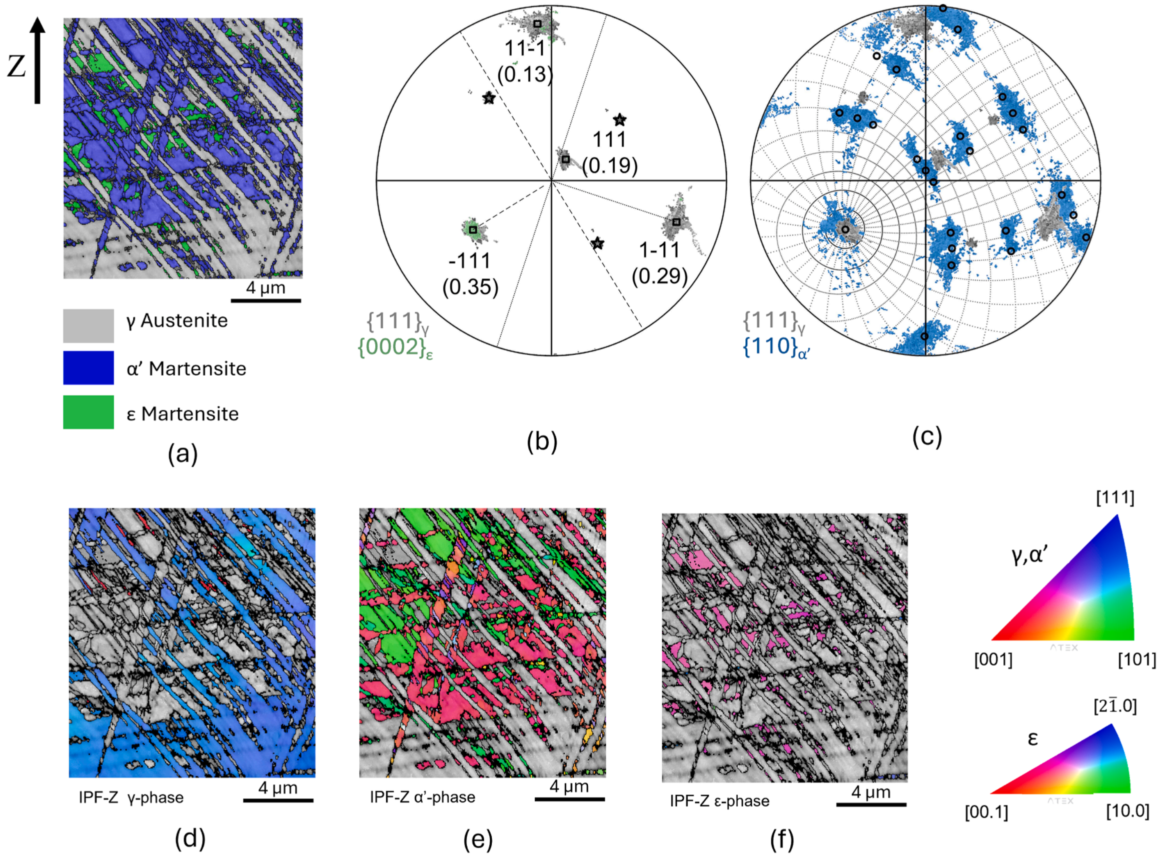

Fig. 7. EBSD phase map and related pole figures carried out at a depth of 100 µm from the CT treated surface (a) EBSD map with the austenite in grey, ε-martensite in green and α'-martensite in blue. (b) Pole figure of the {111}γ-austenite (grey, ☐), the related twin poles (grey, ☆) and the {00.2}ε-martensite (green). Dashed lines represent the plane traces of the two {111}γ having the highest Schmid factor (values in parentheses). (c) Pole figure of the {111}γ (grey), the {110}γ' (blue) and the related [$\bar{1}$11]γ α'-martensite variants (○); (d,e,f) IPF representations along the Z-axis for the γ-austenite, γ'-martensite and ε-martensite, respectively.

confirming the (ε/α') $\{0002\}_{\varepsilon}//\{110\}_{\alpha'}$ $<11\bar{2}0>_{\varepsilon}//<1\bar{1}1>_{\alpha'}$ Burgers OR. The α' variants are clearly related to the $(\bar{1}11)_{\gamma}$ most active habit plane of the austenite grain.

Fig. 8 shows EBSD acquisitions carried out at a depth of 125 µm for the RT and 773 K SMATed samples. The images are GND density maps with the presence of twins drawn in red colour. Concerning the deformation mechanisms triggered at this depth, no martensite was detected for both temperature conditions. Numerous mechanical twins can be seen in the sample subjected to SMAT at RT (Fig. 8a). The bright areas in the GND density plot indicate regions with high GND density. They correspond to traces of planar defects on the {111} planes identified from the orientation results. These planar defects are likely to be mechanical twins that are too thin to be indexed with the 50 nm measurement step size [48]. After SMAT at 773 K, it was possible to detect a very small number of twins aligned with the {111} plane traces (Fig. 8b). The structures depicted by the GND density are less planar compared to the RT treatment suggesting fairly dense dislocation entanglement structures along {111} planes. Thus, at RT, mechanical twins accommodate most of the deformation, while at 773 K the deformation is mainly accommodated by dislocation glide with some limited amount of deformation twin.

3.3. Hardness, residual stress, and FWHM gradients

Fig. 9 shows the surface and sub-surface hardness data obtained on the SMATed samples for the different process temperatures. All treatments allow to increase the hardness of the initial material, with a maximum at the treated surface followed by a gradual decrease towards the initial hardness value of the core (172 ± 10 HV). The maximum surface hardness of 485 HV is reached by the CT sample which corresponds to an increase in hardness of + 315 HV. At higher temperatures, the surface hardnesses are lower than at CT but appear to be rather comparable with each other. Values of 435, 421, and 407 HV are measured (standard deviation about ± 20 HV) for the RT, 523 K, and 773 K samples, respectively. These conditions still represent an increase of about + 250HV of the initial hardness.

Below the top surface, from 0 to 220 µm, increasing the temperature leads to a decrease in hardness values until a common inflection point is reached at a depth of 220 µm and a hardness of ~280 HV. From this depth, a crossover is reached and a reverse trend is observed: the warmest treatments generate higher in-depth hardness values. As a consequence, the SMAT temperature also has an effect on the hardened layer thickness estimated to be 500, 600, 650, and 800 µm for the CT, RT, 523 K, and 773 K samples. Thus, warm SMAT results in an increase of the harden depth to the detriment of the surface hardness values.

Fig. 10 shows the evolution of the residual stresses as a function of the depth for the samples SMATed at the different temperatures. The SMAT induced a compressive residual stress gradient along the affected layer with a maximum below the surface. Additionally, the standard deviation associated with the measurement increases with the depth probably because of an increase in grain size. For the CT SMATed sample, a distinction is done between the measurement carried out for the martensitic phase (hollow signs) and the austenite (solid signs) along the first 170 microns.

At the surface, the compressive residual stress value is maximum in the martensite phase at CT with a value of −720 MPa. The γ-CT, RT, and 523 K treatments have comparable intermediate surface residual stress values of −480 MPa, −514 MPa, and −500 MPa, respectively. For the

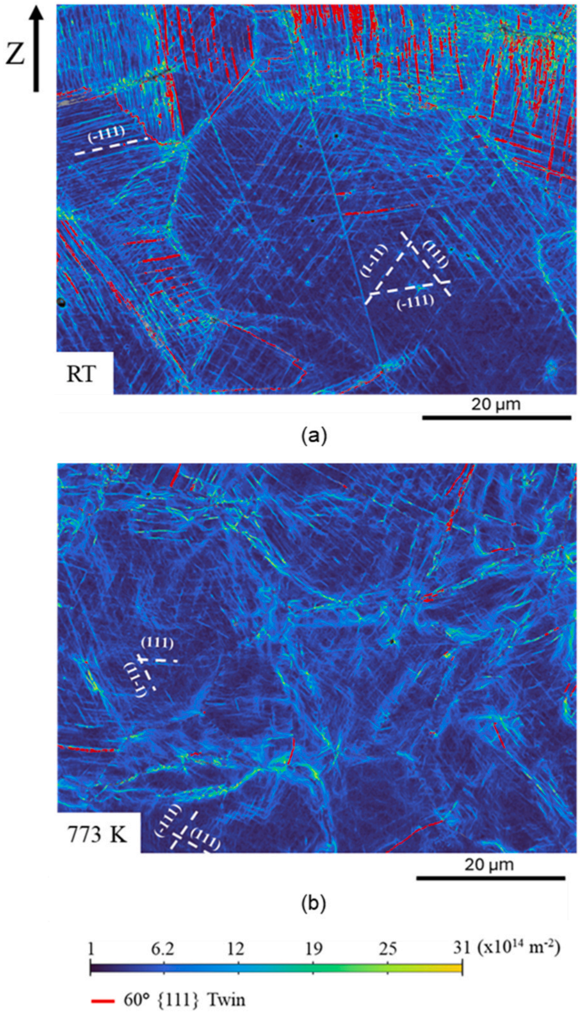

Fig. 8. EBSD maps taken at a depth of 125 µm in the (a) RT sample (b) 773 K sample representing GND density with in red the 60°{111} twin boundaries. The {111} plane traces plotted in white dotted lines were deducted from the crystal orientation obtained by EBSD.

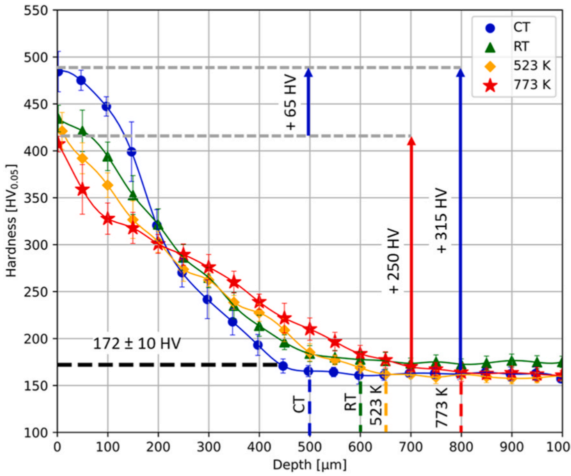

Fig. 9. Vickers hardness as a function of the depth after SMAT at CT (blue), RT (green), 523 K (yellow), and 773 K (red). The horizontal dashed line at 170 HV represents the initial hardness of the material. Error bars represent ± 1 standard deviation from the mean value (n = 10).

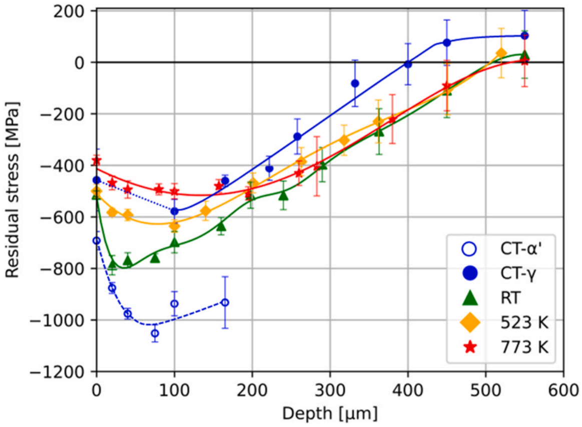

Fig. 10. Residual stress as a function of the depth after SMAT at CT (blue), RT (green), 523 K (yellow), and 773 K (red). Concerning the CT residual stress gradient, the α' martensite and the γ austenite are represented with empty and solid markers, respectively. Error bars represent ± 1 standard deviation from the mean value (n = 5).

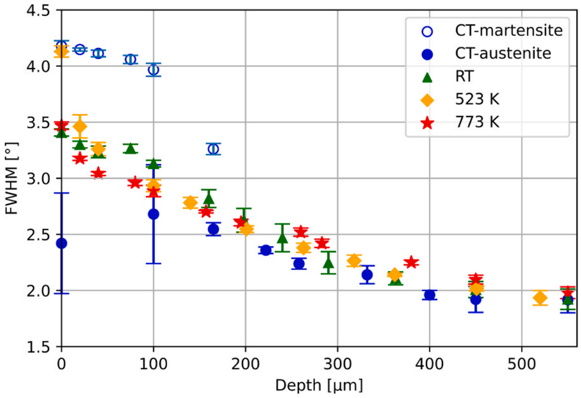

Fig. 11. FWHM as a function of the depth after SMAT at CT (blue), RT (green), 523 K (yellow), and 773 K (red). Concerning the CT FWHM gradient, the α' martensite and the γ austenite are represented with empty and solid markers, respectively. Error bars represent ± 1 standard deviation from the mean value (n = 5).

773 K SMATed sample, the value of surface residual stress (−380 MPa) is half the one obtained under CT condition within the martensite phase.

Below the surface, residual stress gets more compressive with a maximum value of −1050 MPa at a depth of 70 µm for the CT condition. SMAT carried out at RT and 523 K generate lower maximum compressive residual stresses with values of −788 MPa and −635 MPa, respectively. Contrary to the CT and RT samples which show an abrupt drop transition at a low depth (below 100 µm), both warm conditions provide a smoother transition. Ultimately at 773 K, the residual stress gradient can be described as a shallow plateau having residual stress values remaining below −400 MPa down to a depth of about 300 µm. Below 200 µm, no significant difference is observed among the SMAT done at RT, 523 K, and 773 K and the compressive stress states are maintained down to 500 µm. Comparatively, the compressive state is only maintained over 400 µm for CT sample.

Fig. 11 shows the FWHM values extracted from the residual stress peak measurements for all conditions. Indeed, the FWHM values for the different treatment temperature conditions can be documented in order to qualitatively describe the variations of dislocation densities and coherently diffracting domain sizes. Higher FWHM corresponds to higher dislocation densities or smaller domains [49]. The maximum values of FWHM are observed near the surface and then decrease with

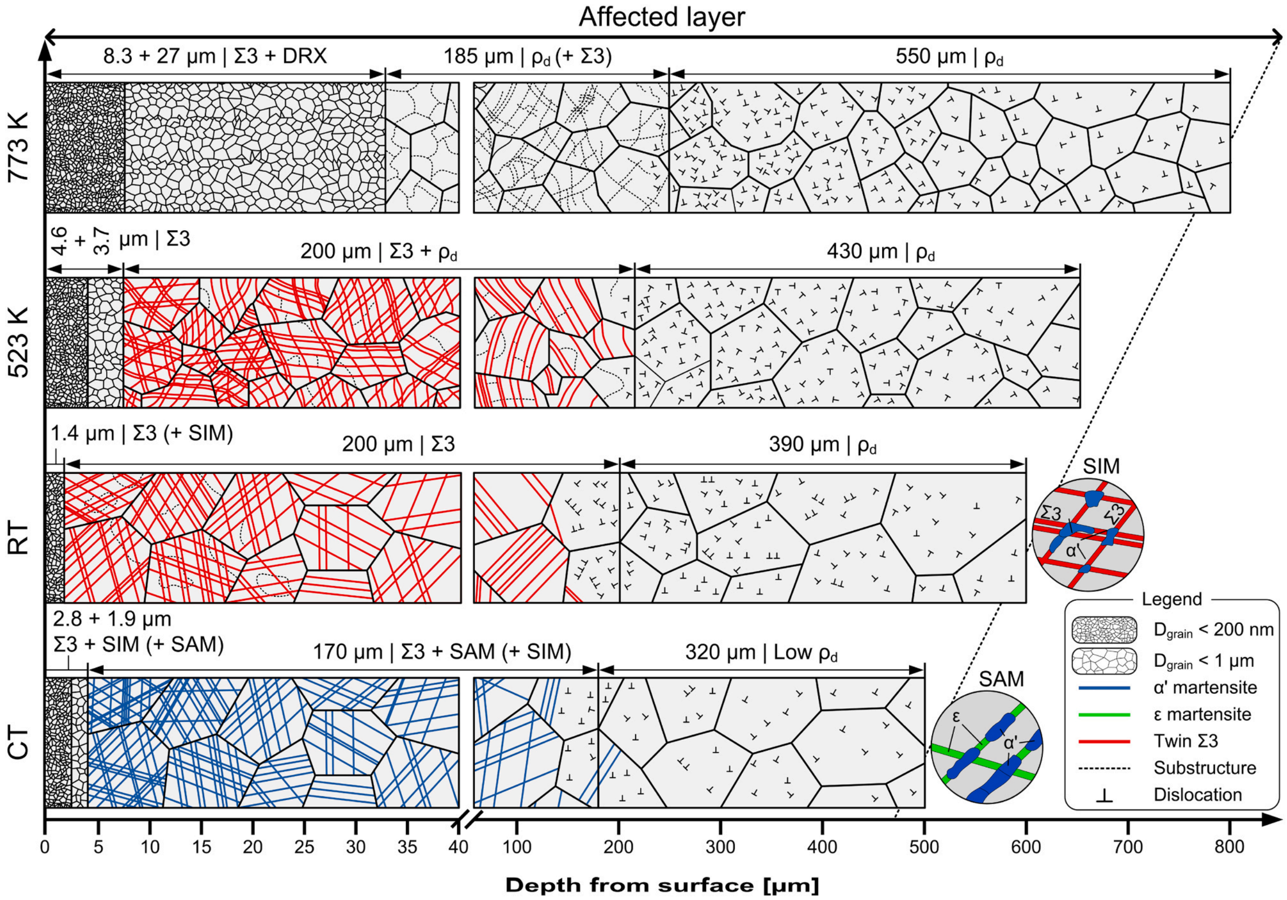

Fig. 12. Mechanisms accommodating the deformation during SMAT at different treatment temperatures and associated thicknesses of the 3 conventional layers. Σ3: mechanical twinning, ρ_d: dislocation density, DRX: dynamic recrystallisation, SAM: stress-assisted martensite, SIM: strain-induced martensite. The mechanisms present in parentheses are reported as additional mechanisms.

the depth, except for the γ phase in the CT condition. This exception can be explained by the large error associated with the measurements due to the weak intensity of the peak.

For the CT sample, at the sample surface, the FWHM in the martensite phase reaches a maximum of about 4.2° and decreases to 3.2° at 180 μm depth. The FWHM values in the austenite - associated with acceptable error values - are much lower. For the other SMAT temperatures, the maximum FWHM values reached at the sample surface are about 3.4°, 4.1°, and 3.5° for RT, 523 K, and 773 K, respectively. The surface FWHM value obtained at 523 K is particularly high. This may be related to a combination of high dislocation density reached at the sample surface, achieved by the combination of twinning and dislocation glide, together with relatively small diffraction regions. Globally, the warmer the SMAT temperature, the smaller the FWHM is along the first ~220 μm. Below this depth, although the FWHM evolutions are rather similar for all the treatment conditions, the trend is inverted and warmer SMAT result in higher FWHM values.

4. Discussion

The microstructural evolution of a 316 L deformed under SMAT in a temperature range from cryogenic condition (~143 K) to 773 K has revealed that the material accommodates the deformation via a large range of mechanisms depending on the temperature and the depth from the treated surface. To illustrate the following discussion, the major observations are gathered in Fig. 12 where the various layer thicknesses and microstructures are recalled and schematised. The nanolayer and UFG layer thicknesses were determined using the EBSD maps (Fig. 5) with a grain size criteria of < 200 nm and < 1 μm, respectively. The TL thicknesses were estimated based on the SEM micrograph observations (Fig. 3). Finally, the PDL thicknesses were defined as the depth when the hardness gradients reach the initial value (Fig. 9).

The first part of the discussion will detail the role of the temperature regarding the mechanisms triggered to accommodate the deformation, while the second part will focus on the effect of the imparted strain on the evolution of the mechanical characteristics (hardness and residual stress) along the affected gradient.

4.1. Effect of SFE on the interplay between the different deformation modes

Varying the SMAT temperature from CT to 773 K is a way to change the SFE of 316 L from 6 to 69 mJ·m^{-2} and consequently influences the deformation mode triggered. At low SFE (6 mJ.m^{-2}, CT), the high strain rate generated by SMAT at the sample surface provides the conditions to induce mechanical twinning [50,51] and these mechanical twins can act as α'-martensite embryos [52,53]. This strain-induced α'-martensite transformation takes place without the formation of ε-martensite (Figs. 5 and 6) [52]. As strain rate decreases with depth, the density of available nucleus for the formation of SIM decreases and martensite will form through the conditions for SAM mechanism [36]. Deeper in the material at about 100 μm depth, some ε-martensite was indeed observed together with the α'-martensite, suggesting that the mechanism leading to the formation of the α'-martensite has changed. The ε-martensite could be described with Nishiyama ORs, suggesting a formation through SAM [51]. The Kurdjomov-Sachs ORs were associated with formation of the α'-martensite, still supporting the SIM formation (Fig. 7b). Under subsequent deformation, the ε-martensite phase will generate some α’-martensite at the intersection laths [53,54] or inside a single ε-lath [55]. In this condition, it is the Burgers ORs that were expected [56] and reported here (Fig. 7).

Surprisingly, the amount of martensite formed after 10 min of SMAT at CT is rather low at the surface area and at 100 μm depth (with 18 % and 40 %, respectively) compared to the calculated M_{d30} value of 278 K estimated from [40], showing that after 10 min of SMAT, the accumulated local strain on the sample surface is still relatively low. The martensite amount depends on the peening duration with an increase of martensite amount with time [36]. Novelli *et al.* found that under similar processing condition and with a material having an equivalent SFE (6 mJ.m^{-2} for a 304Lstainless steel at 193 K), the maximum subsurface amount of martensite went from about 30 % after 3 min processing to 100 % after 20 min treatment. Here, the relatively brief SMAT duration (10 min) and the sample rotation reduce significantly the cumulated strain and the possibility to maximise the amount of martensite. The higher amount of martensite reached in the subsurface area at 100 μm can be attributed to a combination of mechanisms [36]: (i) a higher shear stresses below the surface as expected from the Hertzian contact stress, (ii) the local heating due to the shot impacts increasing the required energy for transformation and (iii) a possible reversion of the martensite when generated at high strain [57,58] due to its lower stability when the grain size decreases significantly. Further away from the surface, the available deformation energy decreases together with the strain rate, so that the critical stress for martensite transformation is not reached, and dislocation activity is the only mechanism available for accommodating the deformation.

For intermediate SFE (23 mJ.m^{-2} and 44 mJ.m^{-2} related to RT and 523 K, respectively) and close to the surface where the strain rate and the strain amount are high, the deformation takes place with a significant amount of mechanical twins (Fig. 5d,f) and no sign of martensitic transformation at the surface. For this range of SFE, TWIP is the governing mechanism reported for the deformation of the austenite [48]. Increasing the SFE from 23 to 44 mJ.m^{-2} decreases the mechanical twin activity and increases the contribution of dislocations to deformation, resulting in intergranular fragmentation (Fig. 5). [59]. Consequently, a higher SFE of 44 mJ·m^{-2} led to an intensive grain refinement on a thicker depth resulting in a thicker UFG layer (Fig. 5). Additionally, shear bands were generated for this SFE, and they were associated with a significant refinement of the microstructure (Fig. 5e). The localised deformation resulting from shear bands formation have been associated with local temperature increase that led to condition where recrystallisation can take place [60], but higher temperature are usually associated with higher grain size. One can argue that adiabatic condition will prevail in shear bands and that it is the local higher strain rates that will control the grain size in this region [61]. Shear bands formation was observed at RT in a 316 L SMATed at lower SFE (18 mJ·m^{-2}) when using larger shots and longer treatment duration that in the present work [60]. The highest available mechanical energy in their condition can explain why this mechanical instability were achieved at lower temperature. Far from the surface, as the strain and strain rate are low, the critical stress for twin nucleation is not reached and deformation is accommodated through dislocation activities.

At high SFE (i.e. at 773 K), the plastic deformation is essentially controlled by dislocation activity over the entire microstructural gradient and the displacive mechanisms discussed before are drastically reduced. This is clearly seen when comparing the microstructure below 125 μm depth, Fig. 8a,b, where the planar defects observed at RT are replaced by disorientated substructures and higher dislocation density, even if the processing temperature is significantly higher and dynamic restoration processes are expected. As dislocation glide is promoted, the UFG layer is expanded down to 35 μm below the treated surface (Fig. 12) and some evidence of Dynamic Recrystallisation (DRX) can be seen. The presence of twins at grain boundaries in Fig. 6d shows that discontinuous recrystallisation takes place through the nucleation of new strain-free grains generated by growth twins. This nucleation mechanism is classically reported in face-centered cubic low SFE material [62,63]. These grains will be progressively deformed by the following shot impacts, generating dislocation substructures and inducing grain rotation. These rotations will reduce the coherency of the twin relationship as illustrated in Fig. 6d. The occurrence of dDRX is also supported by the random texture found at the sample surface, as the formation of growth twins tends to randomise the overall texture [63]. The presence of dislocation substructures in the formed microstructures may also suggest the occurrence of continuous Dynamic Recrystallisation (cDRX) as reported for some austenitic stainless steel subjected to warm deformation [64,65]. Thus, a competition between the dDRX and the cDRX mechanisms may take place under SMAT done at 773 K.

To summarise, the TRIP mechanism which controls the deformation under low SFE (low SMAT temperature) and results in a large amount of ε and α’-martensite switches to a TWIP mechanism, as the SFE (and SMAT temperatures) increases up to 44 mJ.m^{-2} (523 K). Deformation finally relies on dislocation activities and dynamic restoration processes for higher SFE encountered under warm SMAT (773 K), and eventually in DRX at the sample surface, responsible for the flow-like morphology observed along the first 35 μm.

4.2. *Effect of strain and mechanisms on the hardness and residual stress gradients*

As the imparted strain triggers various mechanisms, the origin of the generated hardness and residual stresses gradients changes with the SMAT processing temperature. The microhardness filiations presented in Fig. 9 and the residual stress gradients in Fig. 10 are the consequence of the complex in-depth heterogeneous deformation of the microstructure.

The very top surface (the first microns) is characterized by very high strain rates and large local accumulated strains, resulting in an extensive grain refinement for all the processing conditions (Figs. 4 and 5). The refinement mechanisms differ but the final grain sizes are comparable (Fig. 6). In the CT sample, a notable increase in top surface hardness is obtained (485 HV) in comparison to the other peening conditions (~420 HV). This is clearly due to the presence of the second phase α’-martensite. This phase takes the form of equiaxed grain at the topmost surface and in very fine slip bands deeper, acting as a barrier to dislocation motion [66,67]. For the RT, 523 K and 773 K conditions, the surface hardness is controlled by the grains size and dislocation density as no martensite is present. The surface FWHM (Fig. 11) is similar for the RT and 773 K but significantly higher for the 523 K sample. This suggests a combination of high dislocation density and small diffracting domains, both contributing to the large FWHM value for the 523 K. This condition may be attributed to the combined accumulation of dislocations and warmer temperature activating restoration processes, both contributing to a large FWHM value. In comparison, the lower peening temperature prevents the formation of coherent diffracting domains while the higher one restores excessively the dislocation structures.

For the subsurface hardnesses values, the presence of a significant amount of martensite in the sample processed at CT results in a much harder microstructure along the first 200 μm (Fig. 9). However, higher amount of martensite phase does not necessarily correspond to higher hardness values. Indeed, the percentage of martensite is higher 100 μm below the surface than at the top surface. For the other conditions, as TRIP mechanism is one of the active deformation process, colder deformation facilitates its contribution to strain hardening leading to the superior hardnesses values for the RT sample. In addition, the temperature increase promotes dislocation glide, recovery, and eventually recrystallisation, resulting in dislocation annihilation. This is illustrated by the lower FWHM values reached in warm SMATed samples (Fig. 11) and the formation of coarser substructures (Fig. 8).

Interestingly, the hardness cross-over observed at a depth in the vicinity of 220 μm (at about 280 HV) in Fig. 9 corresponds to the end of the UFG + TL regions (Figs. 3 and 12) where displacive defects formation controls the deformation process and significant strain hardening can be achieved. Below this cross-over (depth > 220 μm) the absence of displacive defects reduce the potential strain hardening of the material, which is controlled only by dislocation activity and the effect of temperature on the onset of plasticity.

The yield stress of 316 L austenitic stainless steel was documented by Molnár *et al.* [59]: 278 MPa at RT, 190 MPa at 523 K, and 158 MPa at 773 K; giving an activation energy of 174 kJ.mol^{-1} (using a strain rate coefficient of 0.013 [68]). Considering that the kinetic energy of the shots is the same for the different SMAT conditions, the decrease in yield stress allows an increase of the depth at which the deformation can take place. The hardened surface layer also influences the energy transfer in the subsurface region during the SSPD process [10]. Thus, the very hard surface generated during cryogenic SMAT consumes a significant amount of energy, impeding deeper hardening. On the other hand, the softer surface in warm conditions allows a more uniform plastic deformation in the PDL layer. Thus, increasing the SMAT temperature facilitates dislocation activity in the PDL region (>220 μm) resulting in higher dislocation densities and deeper affected zones under warm SMAT conditions (Fig. 4g,h). These changes in preponderant hardening mechanisms inducing a crossover in Fig. 9 is also reflected by a concomitant crossover in values of FWHM (Fig. 11). Indeed, at the exception of the CT condition for which martensite has formed, the trends on the effect of SMAT temperature on FWHM is also changed at about 200 μm depth. Below 200 μm, the more intense dislocation activities under warmer conditions is reflected by higher values of FWHM and higher hardness values.

The residual stress evolution can also be explained by the deformation gradient generated during the SSPD process. As residual stresses are controlled by the heterogeneous nature of the deformation introduced by the manufacturing process, it is expected that the maximum residual stress located in the subsurface area coincides with the region where the maximum of deformation occurred. Significantly higher compressive values are found when the α'-martensite phase is formed (CT sample) due to 2 % volume expansion associated with the formation of this phase [69]. Similarly, higher compressive residual stress values are reached in the martensite phase than in the austenite phase (Fig. 10) in the region where both phases can be measured (between 100 and 180 μm). This difference can be explained by the volume change associated with phase transformation and the higher yield strength of the martensite phase, which can build higher residual stresses [70]. Increasing the peening temperature to RT leads to a drastic reduction of martensitic transformation (Fig. 5), leading to a lower maximum of compressive residual stress. For warmer conditions (523 K and 773 K), the thermally activated recovery process result in less significant residual stress as display in Fig. 10. Similarly to the hardness evolution and for the same reasons, all conditions reached almost the same residual stress value of 500 MPa at 220 μm depth.

After this depth, the residual stress linearly decreases for all the samples towards the tensile balancing region. In this domain, the strain heterogeneities leading to the compressive residual stress can only be attributed to the introduced dislocation (Fig. 12), explaining the shorter compressive domain for the CT condition, as dislocation activity is limited at this temperature.

While the formation of α'-martensite under cryogenic conditions enhances hardness and compressive residual stresses, it is essential to acknowledge its potential drawbacks. Since martensite forms during the SMAT process, the scope for further phase transformation under mechanical loading (e.g., fatigue) becomes limited. This can reduce the high ductility characteristic of austenitic stainless steel, potentially leading to earlier fatigue failure [71].

Martensite formation can negatively impact the corrosion resistance of austenitic stainless steels [72], which is one of their key advantages in various industrial applications. Therefore, the introduction of martensitic phases to improve surface properties should be carefully evaluated, considering the specific application requirements and potential trade-offs.

5. Conclusions

This study has demonstrated the significant influence of the temperature at which the Surface Mechanical Attrition Treatment (SMAT) is carried out.

The metastable 316 L alloy exhibited a wide spectrum of deformation mechanisms influenced by the SMAT temperature. Cryogenic peening (143 K) favoured transformation induced plasticity, while moderate temperatures (up to 523 K) activated twinning-induced plasticity. At high temperatures (773 K), the peening deformation was primarily accommodated through dislocation glide. Across all SMAT conditions, the treated surface exhibited the characteristic tri-layered structure: ultrafine-grained (UFG) surface layer, transition layer (TL), and plastically deformed layer (PDL). However, the thickness of these layers varied significantly with the peening temperature. This temperature-dependent shift underscores the ability to manipulate deformation pathways to achieve desired microstructure gradients having different mechanical properties.

The hardness and residual stress values in the subsurface (UFG+TL layers) are controlled by displacive deformation mechanisms, potentially accompanied by DRX at high SMAT temperature while the in-depth properties (PDL layer) are solely controlled by dislocation activity. Under cryogenic condition, SAM and SIM martensites were formed and the ε → α' Burgers, γ → ε Nishiyama and γ → α' Kurdjomov-Sach ORs were identified. The presence of α'-martensite allows a notable increase in surface and subsurface hardnesses as well as compressive residual stress to the detriment of penetration depth. The surface hardness could reach 485 HV (for a 4.7 μm thick ultrafine grain layer) and very high compressive residual stresses (-1000 MPa) at around 100 μm below the surface.

Under warm condition (773 K), the surface hardness and compressive residual stress values were lower to 400 HV and −500 MPa, respectively. A much thicker layer of UFG domain extending down to 35 μm and compressive residual stresses extending as deep as 550 μm were produced. The residual stress remains below −400 MPa even at a depth of 300 μm.

The interplay between the various deformation mechanisms generates microstructure evolutions and associated hardness / residual stress gradients which may offers opportunities for tailoring material properties based on a proper selection of the peening temperature.

CRediT authorship contribution statement

Bocher Philippe: Writing – review & editing, Supervision, Conceptualization. **NOVELLI Marc:** Writing – review & editing, Writing – original draft, Supervision, Conceptualization. **Grosdidier Thierry:** Writing – review & editing, Supervision, Conceptualization. **Austernaud Yann:** Writing – review & editing, Writing – original draft, Methodology, Investigation, Conceptualization.

Declaration of Competing Interest

The authors declare that they have no known competing financial interests or personal relationships that could have appeared to influence the work reported in this paper.

Acknowledgments

This study was also supported in part by the French State through the program “Investment in the future” operated by the National Research Agency (ANR) and referenced by ANR-11- LABX-0008-01 (Labex DAMAS).

Data availability

The data that support the findings of this study are available from the corresponding author upon reasonable request.

References

[1] Edalati, K., Bachmaier, A., Beloshenko, V.A., Beygelzimer, Y., Blank, V.D., Botta, W.J., Bryła, K., Čížek, J., Divinski, S., Enikeev, N.A., Estrin, Y., Faraji, G., Figueiredo, R.B., Fuji, M., Furuta, T., Grosdidier, T., Gubicza, J., Hohenwarter, A., Horita, Z., Huot, J., Ikoma, Y., Janeček, M., Kawasaki, M., Král, P., Kuramoto, S., Langdon, T.G., Leiva, D.R., Levitas, V.I., Mazilkin, A., Mito, M., Miyamoto, H., Nishizaki, T., Pippan, R., Popov, V.V., Popova, E.N., Purcek, G., Renk, O., Révész, Á., Sauvage, X., Sklenicka, V., Skrotzki, W., Straumal, B.B., Suwas, S., Toth, L.S., Tsuji, N., Valiev, R.Z., Wilde, G., Zehetbauer, M.J., Zhu, X., 2022. Nanomaterials by severe plastic deformation: review of historical developments and recent advances. Mater. Res. Lett. 10, 163–256. https://doi.org/10.1080/21663831.2022.2029779.

[2] Grosdidier, T., Novelli, M., 2019. Recent developments in the application of surface mechanical attrition treatments for improved gradient structures: processing parameters and surface reactivity. Mater. Trans. 60, 1344–1355. https://doi.org/10.2320/matertrans.MF201929.

[3] Bagheri, S., Guagliano, M., 2009. Review of shot peening processes to obtain nanocrystalline surfaces in metal alloys. Surf. Eng. 25, 3–14. https://doi.org/10.1179/026708408X334087.

[4] Zhang, C., Dong, Y., Ye, C., 2021. Recent developments and novel applications of laser shock peening: a review. Adv. Eng. Mater. 23, 2001216. https://doi.org/10.1002/adem.202001216.

[5] Grosdidier, T., Zou, J.X., Bolle, B., Hao, S.Z., Dong, C., 2010. Grain refinement, hardening and metastable phase formation by high current pulsed electron beam (HCPEB) treatment under heating and melting modes. J. Alloy. Compd. 504, S508–S511. https://doi.org/10.1016/j.jallcom.2010.04.010.

[6] Kishore, A., John, M., Ralls, A.M., Jose, S.A., Kuruveri, U.B., Menezes, P.L., 2022. Ultrasonic nanocrystal surface modification: processes, characterization, properties, and applications. Nanomaterials 12, 1415. https://doi.org/10.3390/nano12091415.

[7] Chakkravarthy, V., Manojkumar, P., Jerome, S., Evlashin, S.A., Arackal Narayanan, J., Mendagaliev, R.V., Sidorenko, A.O., Narayan, R.L., 2024. Effect of impact angle on hot corrosion resistance of abrasive water jet peened Ti-6Al-4V alloy. Surf. Coat. Technol. 494, 131523. https://doi.org/10.1016/j.surfcoat.2024.131523.

[8] Azadmanjiri, J., Berndt, C.C., Kapoor, A., Wen, C., 2015. Development of surface nano-crystallization in alloys by surface mechanical attrition treatment (SMAT). Crit. Rev. Solid State Mater. Sci. 40, 164–181. https://doi.org/10.1080/10408436.2014.978446.

[9] Lu, K., Lu, J., 2004. Nanostructured surface layer on metallic materials induced by surface mechanical attrition treatment. Mater. Sci. Eng.: A 375–377, 38–45. https://doi.org/10.1016/j.msea.2003.10.261.

[10] Liu, J., Ye, C., Dong, Y., 2020. Recent development of thermally assisted surface hardening techniques: a review. Adv. Ind. Manuf. Eng., 100006 https://doi.org/10.1016/j.aime.2020.100006.

[11] Maleki, E., Unal, O., Guagliano, M., Bagherifard, S., 2022. Analysing the fatigue behaviour and residual stress relaxation of gradient nano-structured 316L steel subjected to the shot peening via deep learning approach. Met. Mater. Int. 28, 112–131. https://doi.org/10.1007/s12540-021-00995-8.

[12] Unal, O., Varol, R., 2014. Almen intensity effect on microstructure and mechanical properties of low carbon steel subjected to severe shot peening. Appl. Surf. Sci. 290, 40–47. https://doi.org/10.1016/j.apsusc.2013.10.184.

[13] Harada, Y., Mori, K., 2005. Effect of processing temperature on warm shot peening of spring steel. J. Mater. Process. Technol. 162–163, 498–503. https://doi.org/10.1016/j.jmatprotec.2005.02.095.

[14] A. Tange, H. Koyama, H. Tsuji, J. Schaad, Study on Warm Shot Peening for Suspension Coil Spring, in: 1999: pp. 1999-01–0415. https://doi.org/10.4271/1999-01-0415.

[15] Tange, A., Ando, K., 2002. Improvement of spring fatigue strength by new warm stress double shot peening process. Mater. Sci. Technol. 18, 642–648. https://doi.org/10.1179/026708302225003514.

[16] Wick, A., Schulze, V., Vöhringer, O., 2000. Effects of warm peening on fatigue life and relaxation behaviour of residual stresses in AISI 4140 steel. Mater. Sci. Eng. A 293, 191–197. https://doi.org/10.1016/S0921-5093(00)01035-2.

[17] Angkurarach, L., Juijerm, P., 2020. Effects of high-temperature deep rolling on fatigue, work hardening, and residual stress relaxation of martensitic stainless steel AISI 420. J. Mater. Eng. Perform. 29, 1416–1423. https://doi.org/10.1007/s11665-020-04656-6.

[18] Amanov, A., Urmanov, B., Amanov, T., Pyun, Y.S., 2017. Strengthening of Ti-6Al-4V alloy by high temperature ultrasonic nanocrystal surface modification technique. Mater. Lett. 196, 198–201. https://doi.org/10.1016/j.matlet.2017.03.059.

[19] Thomas, M., Jackson, M., 2012. The role of temperature and alloy chemistry on subsurface deformation mechanisms during shot peening of titanium alloys. Scr. Mater. 66, 1065–1068. https://doi.org/10.1016/j.scriptamat.2012.02.049.

[20] Zhou, J.Z., Meng, X.K., Huang, S., Sheng, J., Lu, J.Z., Yang, Z.R., Su, C., 2015. Effects of warm laser peening at elevated temperature on the low-cycle fatigue behavior of Ti6Al4V alloy. Mater. Sci. Eng. A 643, 86–95. https://doi.org/10.1016/j.msea.2015.07.017.

[21] Ye, C., Suslov, S., Kim, B.J., Stach, E.A., Cheng, G.J., 2011. Fatigue performance improvement in AISI 4140 steel by dynamic strain aging and dynamic precipitation during warm laser shock peening. Acta Mater. 59, 1014–1025. https://doi.org/10.1016/j.actamat.2010.10.032.

[22] Lim, S.H., Zhang, Z., Seng, D.H.L., Lin, M., Teo, S.L., Wei, F., Cheong, A.K.H., Wang, S., Pan, J., 2021. In-situ warm shot peening on Ti-6Al-4V alloy: effects of temperature on fatigue life, residual stress, microstructure and mechanical properties. J. Alloy. Compd. 882, 160701. https://doi.org/10.1016/j.jallcom.2021.160701.

[23] Liu, J., Suslov, S., Li, S., Qin, H., Ren, Z., Doll, G.L., Cong, H., Dong, Y., Ye, C., 2018. Electrically assisted ultrasonic nanocrystal surface modification of Ti6Al4V alloy. Adv. Eng. Mater. 20, 1–6. https://doi.org/10.1002/adem.201700470.

[24] Liu, J., Suslov, S., Ren, Z., Dong, Y., Ye, C., 2019. Microstructure evolution in Ti64 subjected to laser-assisted ultrasonic nanocrystal surface modification. Int. J. Mach. Tools Manuf. 136, 19–33. https://doi.org/10.1016/j.ijmachtools.2018.09.005.

[25] Amanov, A., Pyun, Y.S., 2017. Local heat treatment with and without ultrasonic nanocrystal surface modification of Ti-6Al-4V alloy: mechanical and tribological properties. Surf. Coat. Technol. 326, 343–354. https://doi.org/10.1016/j.surfcoat.2017.07.064.

[26] Ye, C., Liao, Y., Cheng, G.J., 2010. Warm laser shock peening driven nanostructures and their effects on fatigue performance in aluminum alloy 6160. Adv. Eng. Mater. 12, 291–297.

[27] Pan, X., Wang, X., Tian, Z., He, W., Shi, X., Chen, P., Zhou, L., 2021. Effect of dynamic recrystallization on texture orientation and grain refinement of Ti6Al4V titanium alloy subjected to laser shock peening. J. Alloy. Compd. 850, 156672. https://doi.org/10.1016/j.jallcom.2020.156672.

[28] Kikuchi, S., Tanaka, I., Takesue, S., Komotori, J., Matsumoto, K., 2018. Dynamic recrystallization of Fe-Cr alloys by atmospheric-controlled induction-heating fine particle peening. Surf. Coat. Technol. 344, 410–417. https://doi.org/10.1016/j.surfcoat.2018.03.030.

[29] Lu, J., Hultman, L., Holmström, E., Antonsson, K.H., Grehk, M., Li, W., Vitos, L., Golpayegani, A., 2016. Stacking fault energies in austenitic stainless steels. Acta Mater. 111, 39–46. https://doi.org/10.1016/j.actamat.2016.03.042.

[30] Sun, G., Sun, X., Li, S., Wu, Y., Liu, J., 2022. Effect of rolling temperature on microstructural characteristics and deformation mechanisms of a metastable austenitic stainless steel. Steel Res. Int. 93, 2200096. https://doi.org/10.1002/srin.202200096.

[31] Mosecker, L., Pierce, D.T., Schwedt, A., Beighmohamadi, M., Mayer, J., Bleck, W., Wittig, J.E., 2015. Temperature effect on deformation mechanisms and mechanical properties of a high manganese C+N alloyed austenitic stainless steel. Mater. Sci. Eng.: A 642, 71–83. https://doi.org/10.1016/j.msea.2015.06.047.

[32] Novelli, M., Fundenberger, J.-J., Bocher, P., Grosdidier, T., 2016. On the effectiveness of surface severe plastic deformation by shot peening at cryogenic temperature. Appl. Surf. Sci. 389, 1169–1174. https://doi.org/10.1016/j.apsusc.2016.08.009.

[33] Arifvianto, B., Suyitno, Mahardika, M., Dewo, P., Iswanto, P.T., Salim, U.A., 2011. Effect of surface mechanical attrition treatment (SMAT) on microhardness, surface roughness and wettability of AISI 316L. Mater. Chem. Phys. 125, 418–426. https://doi.org/10.1016/j.matchemphys.2010.10.038.

[34] Roland, T., Retraint, D., Lu, K., Lu, J., 2006. Fatigue life improvement through surface nanostructuring of stainless steel by means of surface mechanical attrition treatment. Scr. Mater. 54, 1949–1954. https://doi.org/10.1016/j.scriptamat.2006.01.049.

[35] Dureau, C., Arzaghi, M., Massion, R., Nadot, Y., Grosdidier, T., 2022. On the high cycle fatigue resistance of austenitic stainless steels with surface gradient microstructures: effect of load ratio and associated residual stress modification. Mater. Sci. Eng.: A 840, 142916. https://doi.org/10.1016/j.msea.2022.142916.

[36] Novelli, M., Bocher, P., Grosdidier, T., 2018. Effect of cryogenic temperatures and processing parameters on gradient-structure of a stainless steel treated by ultrasonic surface mechanical attrition treatment. Mater. Charact. 139, 197–207. https://doi.org/10.1016/j.matchar.2018.02.028.

[37] Bisen, N.S., Sivasubramanian, J., Basu, A., 2023. Ultrasonic shot peening of 316L stainless steel – experimental and analytical approach. Mater. Today. Proc. 91, 1–8. https://doi.org/10.1016/j.matpr.2023.03.751.

[38] P.K, S., D.B, P., Gautam, J., Rai, A.K., Paul, C.P., 2024. Synergistic integration of laser shock peening and heat treatment for refined microstructure and enhanced mechanical properties in additively manufactured 17–4PH stainless steel. J. Mater. Process. Technol. 328, 118395. https://doi.org/10.1016/j.jmatprotec.2024.118395.

[39] Pickering, F.B., 1978. Physical metallurgy and the design of steels. Applied Science Publishers, London.

[40] Angel, T., 1954. Formation of martensite in austenitic stainless steels effects of deformation, temperature, and composition. J. Iron Steel Inst. 177, 165–174.

[41] SONATS, Impact surface treatment solutions and laboratory services, SONATS (2024). ⟨https://sonats-et.com/en/⟩ (accessed January 22, 2024).

[42] Meric de Bellefon, G., van Duysen, J.C., Sridharan, K., 2017. Composition-dependence of stacking fault energy in austenitic stainless steels through linear regression with random intercepts. J. Nucl. Mater. 492, 227–230. https://doi.org/10.1016/j.jnucmat.2017.05.037.

[43] Rémy, L., Pineau, A., Thomas, B., 1978. Temperature dependence of stacking fault energy in close-packed metals and alloys. Mater. Sci. Eng. 36, 47–63. https://doi.org/10.1016/0025-5416(78)90194-5.

[44] B. Beausir, J.-J. Fundenberger, Analysis Tools for Electron and X-ray diffraction, ATEX, (2017). ⟨www.atex-software.eu⟩.

[45] Toth, L.S., Gu, C.F., Beausir, B., Fundenberger, J.J., Hoffman, M., 2016. Geometrically necessary dislocations favor the Taylor uniform deformation mode

in ultra-fine-grained polycrystals. Acta Mater. 117, 35–42. https://doi.org/10.1016/j.actamat.2016.06.062.

[46] Moore, M.G., Evans, W.P., 1958. Mathematical correction for stress in removed layers in x-ray diffraction residual stress analysis. SAE Trans. 66, 340–345.

[47] Samih, Y., Beausir, B., Bolle, B., Grosdidier, T., 2013. In-depth quantitative analysis of the microstructures produced by surface mechanical attrition treatment (SMAT). Mater. Charact. 83, 129–138. https://doi.org/10.1016/j.matchar.2013.06.006.

[48] Barbier, D., Gey, N., Bozzolo, N., Allain, S., Humbert, M., 2009. EBSD for analysing the twinning microstructure in fine-grained TWIP steels and its influence on work hardening. J. Microsc. 235, 67–78. https://doi.org/10.1111/j.1365-2818.2009.03182.x.

[49] Ungár, T., 2001. Dislocation densities, arrangements and character from X-ray diffraction experiments. Mater. Sci. Eng.: A 309–310, 14–22. https://doi.org/10.1016/S0921-5093(00)01685-3.

[50] G.T. Gray III, Deformation twinning: Influence of strain rate, (1993). ⟨https://www.osti.gov/biblio/10193638⟩.

[51] Shen, Y.F., Li, X.X., Sun, X., Wang, Y.D., Zuo, L., 2012. Twinning and martensite in a 304 austenitic stainless steel. Mater. Sci. Eng.: A 552, 514–522. https://doi.org/10.1016/j.msea.2012.05.080.

[52] Olson, G.B., Cohen, M., 1972. A mechanism for the strain-induced nucleation of martensitic transformations. J. Less Common Met. 28, 107–118. https://doi.org/10.1016/0022-5088(72)90173-7.

[53] Fujita, H., Katayama, T., 1992. <I>In-situ< /I> Observation of Strain-Induced γ→ε→α′ and γ→α′ Martensitic Transformations in Fe–Cr–Ni Alloys. Mater. Trans., JIM 33, 243–252. https://doi.org/10.2320/matertrans1989.33.243.

[54] Venables, J.A., 1962. The martensite transformation in stainless steel. Philos. Mag.: A J. Theor. Exp. Appl. Phys. https://doi.org/10.1080/14786436208201856.

[55] Yang, X.-S., Sun, S., Zhang, T.-Y., 2015. The mechanism of bcc α′ nucleation in single hcp ε laths in the fcc γ→hcp ε→bcc α′ martensitic phase transformation. Acta Mater. 95, 264–273. https://doi.org/10.1016/j.actamat.2015.05.034.

[56] Humbert, M., Petit, B., Bolle, B., Gey, N., 2007. Analysis of the γ–ε–α′ variant selection induced by 10% plastic deformation in 304 stainless steel at −60 °C. Mater. Sci. Eng.: A 454–455, 508–517. https://doi.org/10.1016/j.msea.2006.11.112.

[57] Ni, Z., Wang, X., Wang, J., Wu, E., 2003. Characterization of the phase transformation in a nanostructured surface layer of 304 stainless steel induced by high-energy shot peening. Phys. B: Condens. Matter 334, 221–228. https://doi.org/10.1016/S0921-4526(03)00069-3.

[58] Li, J.G., Umemoto, M., Yodaka, Y., Fujisaku, K., Tsuchiya, K., 2008. The dynamic phase transformation and formation of nanocrystalline structure in SUS304 austenitic stainless steel subjected to high pressure torsion. Rev. Adv. Mater. Sci. 18, 577–582.

[59] Molnár, D., Sun, X., Lu, S., Li, W., Engberg, G., Vitos, L., 2019. Effect of temperature on the stacking fault energy and deformation behaviour in 316L austenitic stainless steel. Mater. Sci. Eng.: A 759, 490–497. https://doi.org/10.1016/j.msea.2019.05.079.

[60] Bahl, S., Suwas, S., Ungàr, T., Chatterjee, K., 2017. Elucidating microstructural evolution and strengthening mechanisms in nanocrystalline surface induced by surface mechanical attrition treatment of stainless steel. Acta Mater. 122, 138–151. https://doi.org/10.1016/j.actamat.2016.09.041.

[61] Hines, J.A., Vecchio, K.S., 1997. Recrystallization kinetics within adiabatic shear bands. Acta Mater. 45, 635–649. https://doi.org/10.1016/S1359-6454(96)00193-0.

[62] Sakai, T., Belyakov, A., Kaibyshev, R., Miura, H., Jonas, J.J., 2014. Dynamic and post-dynamic recrystallization under hot, cold and severe plastic deformation conditions. Prog. Mater. Sci. 60, 130–207. https://doi.org/10.1016/j.pmatsci.2013.09.002.

[63] Huang, K., Logé, R.E., 2016. A review of dynamic recrystallization phenomena in metallic materials. Mater. Des. 111, 548–574. https://doi.org/10.1016/j.matdes.2016.09.012.

[64] Tikhonova, M., Belyakov, A., Kaibyshev, R., 2013. Strain-induced grain evolution in an austenitic stainless steel under warm multiple forging. Mater. Sci. Eng.: A 564, 413–422. https://doi.org/10.1016/j.msea.2012.11.088.

[65] Satheesh Kumar, S.S., Vasanth, M., Singh, V., Ghosal, P., Raghu, T., 2017. An investigation of microstructural evolution in 304L austenitic stainless steel warm deformed by cyclic channel die compression. J. Alloy. Compd. 699, 1036–1048. https://doi.org/10.1016/j.jallcom.2016.12.321.

[66] Spencer, K., Embury, J.D., Conlon, K.T., Véron, M., Bréchet, Y., 2004. Strengthening via the formation of strain-induced martensite in stainless steels. Mater. Sci. Eng. A 387–389, 873–881. https://doi.org/10.1016/j.msea.2003.11.084.

[67] Liu, J., Chen, C., Feng, Q., Fang, X., Wang, H., Liu, F., Lu, J., Raabe, D., 2017. Dislocation activities at the martensite phase transformation interface in metastable austenitic stainless steel: an in-situ TEM study. Mater. Sci. Eng.: A 703, 236–243. https://doi.org/10.1016/j.msea.2017.06.107.

[68] Güden, M., Enser, S., Bayhan, M., Taşdemirci, A., Yavaş, H., 2022. The strain rate sensitive flow stresses and constitutive equations of a selective-laser-melt and an annealed-rolled 316L stainless steel: a comparative study. Mater. Sci. Eng.: A 838, 142743. https://doi.org/10.1016/j.msea.2022.142743.

[69] Mei, Z., Morris, J.W., 1990. Influence of deformation-induced martensite on fatigue crack propagation in 304-type steels. Met. Trans. A 21, 3137–3152. https://doi.org/10.1007/BF02647310.

[70] D. Kirk, N. Payne, Transformations induced in austenitic stainless steels by shot peening, in: ICSP7: 7th International Conference on Shot Peening Warsaw (Poland), 1999.

[71] Müller-Bollenhagen, C., Zimmermann, M., Christ, H.-J., 2010. Very high cycle fatigue behaviour of austenitic stainless steel and the effect of strain-induced martensite. Int. J. Fatigue 32, 936–942. https://doi.org/10.1016/j.ijfatigue.2009.05.007.

[72] Lv, J., Luo, H., 2014. Effects of strain and strain-induced α′-martensite on passive films in AISI 304 austenitic stainless steel. Mater. Sci. Eng. C. 34, 484–490. https://doi.org/10.1016/j.msec.2013.10.003.